Magnetic excitation spectra in pyrochlore iridates

Eric Kin-Ho Lee,[1] Subhro Bhattacharjee,[1,2] and Yong Baek Kim[1,3]
[1]*Department of Physics and Centre for Quantum Materials, University of Toronto, Toronto, Ontario, Canada M5S 1A7*
[2]*Department of Physics and Astronomy, McMaster University, Hamilton, Ontario, Canada L8S 4M1*
[3]*School of Physics, Korea Institute for Advanced Study, Seoul 130-722, Korea*
(Received 19 November 2012; revised manuscript received 2 May 2013; published 13 June 2013)

Metal-insulator transitions in pyrochlore iridates ($A_2Ir_2O_7$) are believed to occur due to subtle interplay of spin-orbit coupling, geometric frustration, and electron-electron interactions. In particular, the nature of magnetic ordering of iridium ions in the insulating phase is crucial for the understanding of several exotic phases recently proposed for these materials. We study the spectrum of magnetic excitations in the intermediate-coupling regime for the so-called all-in/all-out magnetic state in pyrochlore iridates with nonmagnetic A-site ions (A = Eu,Y). This state was found to be preferred in previous theoretical studies. We find that the effect of charge fluctuations on the magnetic excitations in the intermediate-coupling regime leads to a strong departure from the lowest-order spin-wave calculations based on spin models obtained in the strong-coupling limit. We discuss the characteristic features of the magnetic excitation spectrum that can lead to conclusive identification of the magnetic order in future resonant inelastic x-ray (or neutron) scattering experiments. This knowledge about the nature of magnetic order and its low-energy features may also provide useful information on the accompanying metal-insulator transition.

DOI: 10.1103/PhysRevB.87.214416 PACS number(s): 75.40.Gb, 75.30.Ds, 75.25.−j, 75.10.Lp

I. INTRODUCTION

Pyrochlore iridates ($A_2Ir_2O_7$) have recently attracted much attention as prominent examples of 5*d* transition-metal oxides where interplay of spin-orbit (SO) coupling and electron interactions can lead to a number of competing exotic phases.[1–21] Interestingly, most of these materials are found either to exhibit a finite-temperature metal-insulator (MI) transition[10,11,20,22–26] or to lie naturally close to a zero-temperature MI quantum phase transition (both pressure driven[20,27] and/or chemical-pressure driven via variation of A-site ions[10,22]). It is now believed that the nature of the MI transitions in these systems is related to the magnetic order of iridium ions in the low-temperature insulating phase.[10,24–26] Further, some of the proposed novel phases like the Weyl semimetal depend crucially on the details of such a magnetic ordering pattern.[3,7] Therefore, the determination of the Ir magnetic configuration is important, both to gauge the relevance of the proposed novel phases and to shed light on the character of the MI transition in pyrochlore iridates. However, even for the simpler case of nonmagnetic A-site pyrochlore iridates (such as $Eu_2Ir_2O_7$ and $Y_2Ir_2O_7$), there is no conclusive experimental evidence for the nature of such magnetic order.[11,12,19,22,23,25,28]

Several important clues regarding the magnetic order have been revealed by recent muon spin resonance/relaxation and magnetization measurements on the low-temperature insulating phase of both $Eu_2Ir_2O_7$[11,25] and $Y_2Ir_2O_7$.[19] These measurements suggest that localized Ir moments exhibit long-range magnetic order that may not break the symmetries of the pyrochlore lattice. These results are consistent with the claim that in the ground state, the Ir moments order in the noncollinear, all-in/all-out (AIAO) fashion (see Fig. 1), as was found in previous calculations done in both the strong-[29] and intermediate-electron-correlation regimes.[3,7] However, the above findings cannot conclusively prove that $Eu_2Ir_2O_7$/$Y_2Ir_2O_7$ orders in the AIAO fashion, and a study of the low-energy magnetic excitations is required to identify the signatures unique to the AIAO state. Indeed, recent resonant inelastic x-ray scattering (RIXS) and inelastic neutron-scattering experiments have revealed the magnetic excitation spectra of other iridates such as Sr_2IrO_4,[30] $Sr_3Ir_2O_7$,[31] and Na_2IrO_3,[32] which suggests that the magnetic excitation spectra of pyrochlore iridates can also be probed using these techniques.

In this paper, we compute the magnetic excitation spectrum in both the intermediate- and strong-electron-correlation regimes. Starting from an effective Hubbard model in the $J_{\text{eff}} = 1/2$ basis appropriate for Ir electrons, we study the evolution of the magnetic excitation spectrum in the intermediate-U regime by computing the transverse magnetic dynamical structure factor within the random-phase approximation (RPA). The robust symmetry-protected degeneracies of the magnetic excitation spectrum, the occurrence of Landau damping, and the characteristic dispersion along high-symmetry directions are found to be the defining signatures of the AIAO state in the intermediate-U regime. In the strong-correlation limit, we derive an effective spin model and calculate the corresponding spin-wave excitations. Through fitting of the RPA dynamical structure factor with the strong-coupling spin-wave results, we find that the magnetic excitation spectrum at intermediate U shows strong departures from the lowest-order spin-wave calculations. Since the charge gap estimated from resistivity measurements is found to be small ($\sim$10 meV),[11] the intermediate-coupling regime may be more suitable for describing pyrochlore iridates such as $Eu_2Ir_2O_7$.

The rest of this paper is organized as follows. We begin with a brief description of the Hubbard model relevant to the pyrochlore iridates in Sec. II. We introduce a new parametrization for the tight-binding parameters, which elucidates the structure of the mean-field phase diagram presented in Sec. III. Subsequently, we discuss the results obtained in both the intermediate-U (Sec. IV A) and large-U (Sec. IV B) regimes. We also discuss the unique signatures of the AIAO phase and compare the results obtained in the two different

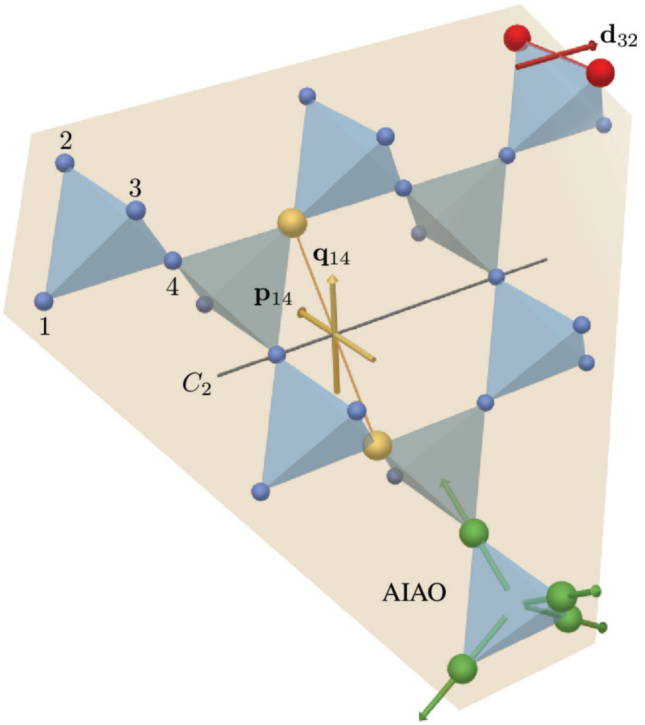

FIG. 1. (Color online) The top left tetrahedron indicates the sublattice indices used in our work. The red vector in the top right tetrahedron shows the nearest-neighbor $\mathbf{d}_{32}$. The gold vectors $\mathbf{p}_{14}$ and $\mathbf{q}_{14}$ are perpendicular to the C_2 axis and span the plane in which next-nearest-neighbor $\mathbf{v}_{\langle\langle 14\rangle\rangle}$ must lie. The bottom right tetrahedron with the green vectors shows the all-in/all-out configuration.

regimes. Implications of our results are summarized in Sec. V. Further details regarding various calculations are given in the appendices.

II. MICROSCOPIC HAMILTONIAN

In the pyrochlore iridates, Ir^{4+} ions are located at the center of corner-sharing oxygen octahedra. This leads to crystal-field splitting of the $5d$ Ir orbitals into upper e_g and lower t_{2g} orbitals. The sixfold-degenerate t_{2g} orbitals (including spin degeneracy) are then split into an upper $J_{\rm eff} = 1/2$ doublet and a lower $J_{\rm eff} = 3/2$ quadruplet by the atomic SO coupling with energy separation of $3\lambda/2$ ($\lambda \approx 500$ meV for Ir). Therefore, in the atomic limit, the five valence electrons will fully fill the $J_{\rm eff} = 3/2$ states, half fill the $J_{\rm eff} = 1/2$ states, and leave the e_g orbitals unoccupied. This atomic picture suggests that the low-energy physics can be captured by projecting out both the $J_{\rm eff} = 3/2$ and e_g states and retaining only the half-filled $J_{\rm eff} = 1/2$ states.[8,9] Therefore it is useful to start from the most general on-site Hubbard model in the $J_{\rm eff} = 1/2$ basis allowed by symmetry:

$$H = \sum_{ij} c_i^\dagger h_{ij} c_j + U \sum_i n_{i\uparrow} n_{i\downarrow}, \tag{1}$$

where i,j are lattice-site indices, $c_i = (c_{i\uparrow}, c_{i\downarrow})$ are the electron annihilation operators, $\uparrow$ and $\downarrow$ are the z components of the pseudospin operator defined in the global basis, and $n_{i\sigma} = c_{i\sigma}^\dagger c_{i\sigma}$ is the electron number operator at site i of pseudospin σ. In general the hopping matrix h_{ij} is complex and can be constrained by considering time-reversal invariance and various space-group symmetries (Moriya rules).[17,29,33]

Time-reversal invariance restricts the hopping matrix to the form

$$h_{ij} = t_{ij}\mathbb{I} + i\mathbf{v}_{ij}\cdot\sigma, \tag{2}$$

where $\mathbb{I}$ is the 2×2 identity matrix, σ $(=\sigma_x,\sigma_y,\sigma_z)$ are the Pauli matrices (in the pseudospin space), and t_{ij} and $\mathbf{v}_{ij} = (\mathrm{v}_{ij}^x,\mathrm{v}_{ij}^y,\mathrm{v}_{ij}^z)$ are real hopping amplitudes. Hermiticity of the Hamiltonian implies

$$t_{ij} = t_{ji}, \quad \mathbf{v}_{ij} = -\mathbf{v}_{ji}. \tag{3}$$

Here t_{ij} and $\mathbf{v}_{ij}$ transform as a scalar and as a pseudovector, respectively, under the space-group symmetries of the lattice.[29,33] In particular these symmetries constrain the nearest neighbor (NN) $\mathbf{v}_{\langle ij\rangle}$ to be perpendicular to the mirror plane containing i and j. The two possible directions in which $\mathbf{v}_{\langle ij\rangle}$ can point are classified as "direct" and "indirect".[29] We shall denote the unit vector of the "direct" case as $\mathbf{d}_{ij}$ (see Fig. 1). For next-nearest neighbors (NNN) $\langle\langle ij\rangle\rangle$, the twofold rotation axis that exchanges i and j restricts $\mathbf{v}_{\langle\langle ij\rangle\rangle}$ to lie in the plane normal to this axis.[34] We can parametrize this plane by the two orthonormal vectors

$$\mathbf{p}_{ij} \equiv \sqrt{6}/4(-\mathbf{R}_{ij} + \mathbf{D}_{ij}), \tag{4}$$

$$\mathbf{q}_{ij} \equiv \sqrt{3}/2(\mathbf{R}_{ij} + \mathbf{D}_{ij}), \tag{5}$$

where $\mathbf{R}_{ij} \equiv \mathbf{r}_{ik}\times\mathbf{r}_{kj}$, $\mathbf{D}_{ij} \equiv \mathbf{d}_{ik}\times\mathbf{d}_{kj}$, site k is the common NN of i and j (see Fig. 1), and $\mathbf{r}_{ik}$ is the vector pointing from site i to k.

The above constraints allow us to parametrize h_{ij} by two real NN (unprimed) hopping amplitudes and three NNN (primed) hopping amplitudes:

$$\begin{aligned} h_{\langle ij\rangle}(t_1,t_2) &= t_1\mathbb{I} + it_2\mathbf{d}_{ij}\cdot\sigma, \\ h'_{\langle\langle ij\rangle\rangle}(t_1',t_2',t_3') &= t_1'\mathbb{I} + i(t_2'\mathbf{p}_{ij} + t_3'\mathbf{q}_{ij})\cdot\sigma. \end{aligned} \tag{6}$$

For the rest of the paper, instead of using $(t_1,t_2),(t_1',t_2',t_3')$ as our hopping parameters, we find it more convenient to work with $(t,\theta),(t',\theta',\phi')$, which makes certain symmetries of the phase diagram readily accessible. These are defined as

$$\begin{pmatrix} t_1 \\ t_2 \end{pmatrix} = t \begin{pmatrix} \cos(\theta_t/2-\theta) \\ \sin(\theta_t/2-\theta) \end{pmatrix}, \tag{7}$$

$$\begin{pmatrix} t_1' \\ t_2' \\ t_3' \end{pmatrix} = t' \begin{pmatrix} \cos(\theta_t/2-\theta')\sin(\phi') \\ \sin(\theta_t/2-\theta')\sin(\phi') \\ \cos(\phi') \end{pmatrix}, \tag{8}$$

where $\theta_t = 2\arctan(\sqrt{2}) \approx 109.47^\circ$ is the tetrahedral angle. This parametrization together with the definition of $\mathbf{p}_{ij}$ and $\mathbf{q}_{ij}$ naturally makes the following property of the model manifest: if we perform the basis transformation $c_{ia\alpha} \to e^{-i\pi\hat{n}_a\cdot\sigma_{\alpha\beta}}c_{ia\beta}$, where $\hat{n}_a$ is the unit vector pointing from sublattice a to the center of the tetrahedron, the hopping parameters θ and θ' are transformed to $-\theta$ and $-\theta'$, respectively. In other words, the Hamiltonian parametrized by hopping parameters $(t,\theta),(t',\theta',\phi')$ yields a spectrum identical to that of the Hamiltonian with parameters $(t,-\theta),(t',-\theta',\phi')$.

We can also derive hopping matrices obeying the above symmetry constraints by considering the Slater-Koster

approximation of orbital overlaps. In terms of this microscopic approach, the relevant Slater-Koster parameters are (1) Ir-Ir hopping via direct overlap of d orbitals [there are three such overlaps: t_σ (for σ bonds), t_π (for π bonds), and t_δ (for δ bonds) for NN (and primed ones for NNN)] and (2) t_o describing the hopping between the Ir atoms via the intermediate oxygen. Details of such a derivation can be found in Refs. 3,6 and 34 and Appendix A.

We now briefly comment on the possible role of trigonal distortion of the octahedral crystal field of oxygen. Since the site symmetry of the Ir^{4+} ions is D_{3d}, trigonal distortion is symmetry allowed, and in principle, one should use the basis orbitals in a trigonal environment. These are the so-called e_g' and a_{1g} orbitals (fourfold and twofold degenerate, including spin degeneracy, respectively). In the presence of trigonal distortions the energies of these two sectors are not equal. This lifting of the t_{2g} orbital degeneracy by trigonal distortion can change the above $J_{\rm eff} = 1/2$ picture if the trigonal distortion energy scale is much larger than the atomic SO coupling.[35] However, when the distortion energy scale is much smaller than the SO coupling, the separation of the e_g' and a_{1g} orbitals is negligible. To a good approximation, one may still use the t_{2g} basis orbitals, consider the strong SO coupling limit first, and treat the trigonal distortion perturbatively. This gives the above $J_{\rm eff} = 1/2$ bands whose mixing with the $J_{\rm eff} = 3/2$ bands is negligible. Treating the trigonal distortion perturbatively in the $J_{\rm eff} = 1/2$ manifold would simply renormalize our hopping parameters and will not change our preceding arguments in an essential way (the $J_{\rm eff} = 1/2$ doublet cannot be split since it is protected by time-reversal symmetry). In the present work, we shall assume that the trigonal distortions in these pyrochlore iridates are small such that the $J_{\rm eff} = 1/2$ atomic orbitals still provide a good description of the low-energy degrees of freedom.

III. MEAN-FIELD PHASE DIAGRAM

In Fig. 2, we show the mean-field phase diagram for $0 < \theta < \pi$. We have chosen $\theta = \theta'$, $t'/t = 0.1$, and $\phi' = 5\pi/6$. The small NNN hopping t' was included to produce the metallic (M), topological Weyl semimetal (TWS), and magnetically ordered metallic (mAIAO) phases, which are otherwise inaccessible with only NN-hopping amplitudes. For $t'/t = 0$ and $U = 0$, the strictly NN-hopping Hamiltonian contains a Kramers pair of identically flat electronic bands at the Fermi level along the Γ-L direction. Inclusion of small t'/t disperses this section of the band structure and produces the aforementioned phases for $U \geqslant 0$.[3,34] Owing to our parametrization, the phase diagram for $0 > \theta > -\pi$ will be identical because of the $(t,\theta),(t',\theta',\phi') \sim (t, -\theta),(t', -\theta',\phi')$ structure, as discussed in Sec. II.

Throughout our calculation we have set $t = 1$ as our energy scale, and we comment on its possible values in physical systems in Sec. V. This is different from Refs. 3 and 34, where the Ir-O-Ir hopping amplitude was used as the unit of energy. In addition, the NNN hoppings in Ref. 34 were chosen differently. Despite these two differences, our phase diagram is in quantitative agreement with that obtained in Ref. 34. This agreement is to be expected since the NNN hoppings are small ($t'/t = 0.1$). We have checked that no new phases are generated with different choices of θ' and ϕ' provided t'/t remains small (as expected in the real materials).

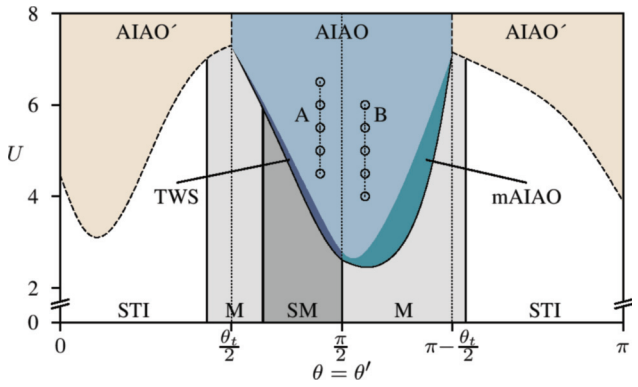

FIG. 2. (Color online) Mean-field phase diagram with hopping amplitudes $\theta' = \theta$, $t'/t = 0.1$, $t = 1$, and $\phi' = 5\pi/6$. First-order transitions are indicated by dashed lines, while second-order transitions are indicated by solid black lines. Lines A ($\theta = 1.45$) and B ($\theta = 1.70$) represent the two cuts for which the RPA dynamical structure factors are calculated (Fig. 3). The phases indicated are strong topological insulator (STI), metallic (M), semimetallic (SM), topological Weyl semimetal (TWS), metallic all-in/all-out (mAIAO), rotated all-in/all-out (AIAO′), and all-in/all-out (AIAO).

In the noninteracting limit, depending on the value of θ, we find the strong topological-insulator (STI), metallic (M), and semimetallic (SM) phases. The M phase has small particle- and holelike pockets, whereas the SM phase has a quadratic band touching at the Γ point at the chemical potential. At finite U, only two magnetic configurations are found: the AIAO and the rotated all-in/all-out (AIAO′) orders.[3] The AIAO configuration is realized by increasing U starting from either the SM or M phase. On the other hand, the AIAO′ configuration is realized by increasing U starting with the M or STI phase. Phase transitions to the AIAO′ by an increase in U are of first order. The transitions between the AIAO and the AIAO′ phases are also of first order and occur at $\theta_t/2$ and $\pi - \theta_t/2$. In the noninteracting limit, band inversion at the Γ point also occurs at these values of θ. All other transitions are of second order.

At large U, the system is gapped, while for values of U near the onset of magnetic order, the single-particle spectrum may continue to remain gapless even after the onset of magnetic order. The TWS and the mAIAO phases are realized in this gapless window: the former is developed via the splitting of the quadratic band touching at the Fermi level of the SM phase, while the latter is realized due to the presence of particle-hole pockets in the M phase.

IV. MAGNETIC EXCITATION SPECTRUM

As pointed out in Sec. III, for a sufficiently large Hubbard interaction U and for $\theta_t/2 < \theta < \pi - \theta_t/2$, the mean-field solution is the AIAO state. We want to study the nature of the low-energy magnetic excitation spectrum of this magnetically ordered state, which is composed of the transverse fluctuations of the spins about their local-ordering directions. We study these excitations in both the intermediate- and strong-electron-correlation regimes, and we accomplish this by applying two contrasting approaches. For the case of intermediate

U, we study the magnetic excitations by computing the RPA transverse spin-spin dynamical structure factor at zero temperature. In the large-U regime, we perform a strong-coupling expansion of our Hubbard model [Eq. (1)] to derive an effective spin model. The spin model is then used to calculate the spin-wave spectrum about the AIAO state within the Holstein-Primakoff approximation.

A. Intermediate U: RPA dynamical structure factor

The information about the magnetic excitations are contained in the transverse part of the RPA dynamical spin-spin susceptibility matrix. This is given by

$$\chi_{\mathrm{RPA}\perp}(\mathbf{q},\omega) = [\mathbf{1} - U\chi_{\mathrm{MF}\perp}(\mathbf{q},\omega)]^{-1}[\chi_{\mathrm{MF}\perp}(\mathbf{q},\omega)], \quad (9)$$

where $\chi_{\mathrm{MF}\perp}$ is the bare mean-field transverse spin-spin susceptibility and U is the Hubbard repulsion. Since the pyrochlore unit cell has four sublattices, $\chi_{\mathrm{MF}\perp}$ is a 4×4 matrix. We compute the trace of the imaginary part of the RPA susceptibility, i.e., the RPA dynamical structure factor. This trace sums over the contribution of the individual magnetic excitation bands (there are four such bands) and gives the overall intensity that will be observed in inelastic neutron-scattering or RIXS experiments. The details of the form of the susceptibility matrix are discussed in Appendix B.

Results. We consider the RPA dynamical structure factor along two representative cuts (A and B) in the phase diagram as U is increased. For cut A, $\theta = 1.45$, while for cut B, $\theta = 1.70$ (Fig. 2). The first cut is chosen to represent the section of the phase diagram given by $(\theta_t/2 < \theta < \pi/2)$, while the second is chosen to represent the part $(\pi/2 < \theta < \pi - \theta_t/2)$. For small NNN hoppings $(t'/t \lesssim 0.1)$ we have explicitly checked that the qualitative features of these representative cuts are robust against variations in t' and θ within their respective sections of the phase diagram (not shown).

Due to the presence of spin-orbit coupling ($t_2 \neq 0$), spin-rotation symmetry is explicitly broken, and the magnetic excitation spectra are generally expected to be gapped. The dynamical structure factors for cut A are shown in Fig. 3(a). For this cut, the system is in the quadratic band-touching SM phase in the noninteracting limit. For $U = 4.5$, the low-lying particle-hole continuum damps and broadens the magnetic excitation spectrum throughout most of the Brillouin zone. This so-called Landau damping occurs because magnetic excitations lying within the particle-hold continuum decay through interactions with the particle-hole excitations. As a consequence, these magnetic excitations acquire a finite lifetime which broadens their spectrum.[36,37] The lower bound of the particle-hole continuum is dispersive, and this is most evident near the L point: the particle-hole excitations are higher in energy than the magnetic excitations; therefore these magnetic excitations

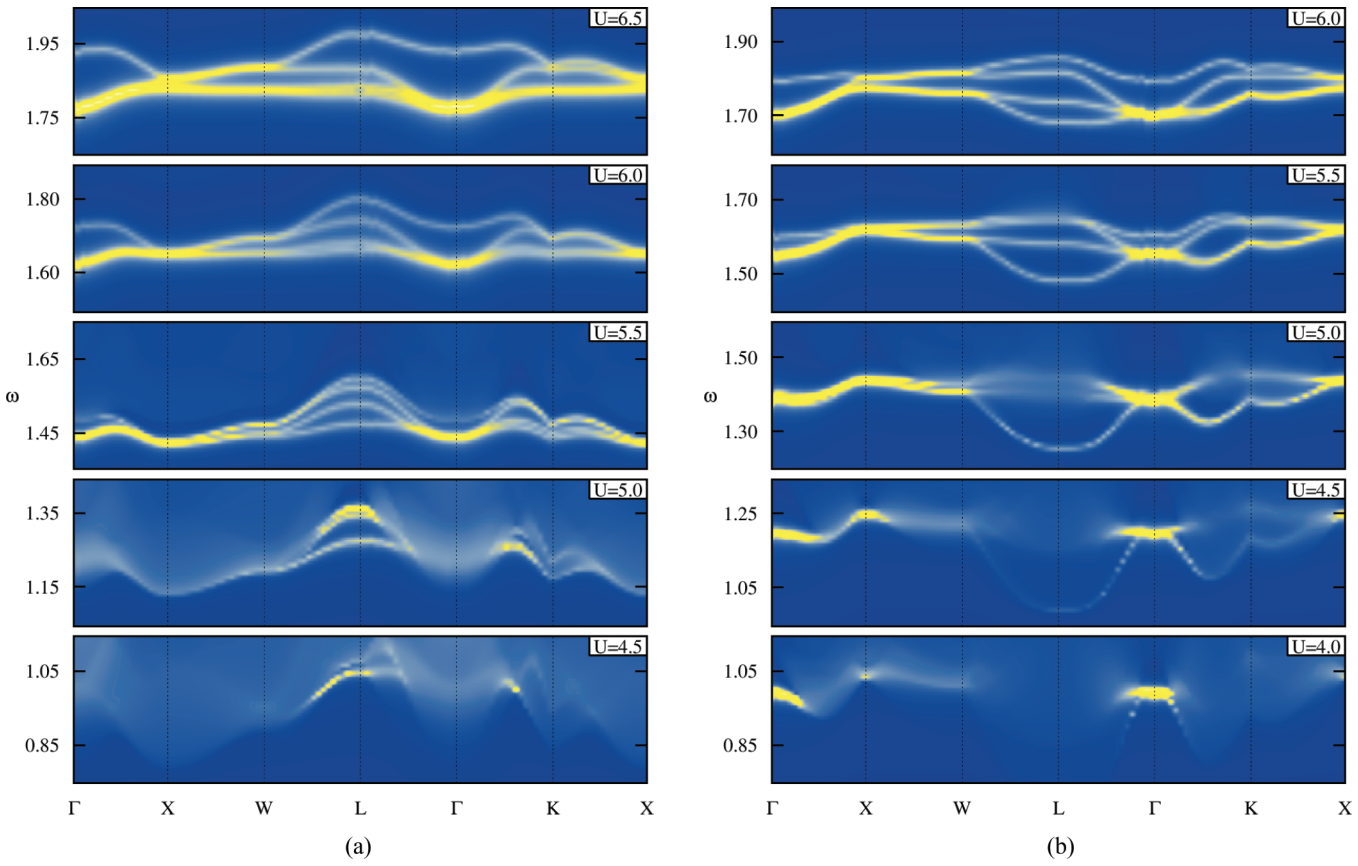

FIG. 3. (Color online) RPA dynamical structure factors for (a) $\theta = 1.45$ and (b) $\theta = 1.70$ for various values of U; ω is in units of $t = 1$. These correspond to cuts A and B in Fig. 2, respectively. Sharp dispersions can be seen at larger values of U, while lighter intensity and broadened spectra are seen due to Landau damping in parts of the Brillouin zone at lower U. Degeneracies at Γ, X, and W are symmetry protected and are robust features of the AIAO state.

become more sharply defined in that region of the Brillouin zone. As U is increased, the particle-hole continuum is shifted upwards in energy throughout the Brillouin zone due to an increase in the single-particle charge gap, hence revealing all four magnetic excitation modes. The lower-energy modes are relatively dispersionless compared to the higher-energy modes, which disperse most markedly near the L point. At $U = 6.5$, the degeneracies of the spectrum become more apparent: there are two twofold degeneracies at the X and W points, while the Γ point has a threefold degeneracy. We note that for $U \lesssim 4.5$, which includes the TWS phase, all the magnetic excitation modes are damped by the particle-hole continuum.

For the second cut [Fig. 3(b)], the system is in the metallic phase in the noninteracting limit. Well-defined magnetic excitations are only observed for $U \gtrsim 4.0$. Starting at $U = 4.0$, the magnetic excitation modes appear near the Γ point. At $U = 4.5$, low-energy, damped features can be seen near the L point and along the Γ-K line. For $U = 5.0$, most of the magnetic excitation modes become sharply defined as the particle-continuum shifts upward. As U is increased further, the low-lying dispersion at L shifts up, and bands at Γ begin to separate while maintaining the threefold degeneracy required by symmetry. At $U = 6.0$, the spectrum begins to resemble the $U = 6.5$ spectrum of the first cut.

Degeneracies at the high-symmetry points Γ, X, and W are symmetry protected, and therefore they are characteristic of the point-group symmetry that remains intact in the AIAO state and common to both cuts A and B at all values of U. The almost flat dispersion encountered at the zone boundary (X-W) is also a distinguishing feature and is also evident in both cuts A and B.

B. Strong-coupling expansion: Linear spin-wave theory

We now look at the spin-wave spectrum in the strong-coupling limit of large U/t. In this limit and at half filling, we can apply perturbation theory to obtain the following effective spin Hamiltonian at the lowest order:[3,6]

$$\begin{aligned} H_{\text{spin}} &= \sum_{ij} \Lambda_{ij}^{ab} S_i^a S_j^b \\ &= \sum_{ij} \left(J \mathbf{S}_i \cdot \mathbf{S}_j + \mathbf{D}_{ij} \cdot \mathbf{S}_i \times \mathbf{S}_j + S_i^a \Gamma_{ij}^{ab} S_j^b \right), \end{aligned} \tag{10}$$

where the three terms in the last line are the trace, traceless antisymmetric, and traceless symmetric parts of Λ_{ij}^{ab}. These terms correspond to the Heisenberg, the Dzyaloshinskii-Moriya (DM), and the anisotropic interactions, respectively, and are related to the hopping amplitudes of Eq. (1) by

$$\begin{aligned} J &= 4U^{-1}(t^2 - |\mathbf{v}|^2/3), \quad \mathbf{D}_{ij} = 8U^{-1} t \mathbf{v}_{ij}, \\ \Gamma_{ij}^{ab} &= 8U^{-1}\left(\mathrm{v}_{ij}{}^a \mathrm{v}_{ij}{}^b - \delta^{ab} |\mathbf{v}|^2/3 \right) \end{aligned} \tag{11}$$

[the magnitude of $\mathbf{v}_{ij}$ ($= |\mathbf{v}|$) is site independent], which holds for both NN- and NNN-hopping amplitudes. The "direct" configuration of the DM vectors are known to stabilize the AIAO state,[29] which is in agreement with our earlier mean-field phase diagram. Hence we consider the low-energy spin-wave expansion about the AIAO state for the above spin Hamiltonian.

To obtain the spin-wave expansion about the AIAO state which orders noncollinearly, we rotate our spin-quantization axis locally in alignment with the magnetic ordering.[38] To this end, we define rotated spin operators $\tilde{\mathbf{S}}$ such that their local S_z points to the direction of magnetic ordering at that site.

$$S_i^a = [\mathbf{R}_i(\tilde{\mathbf{S}}_i)]^a = R_i^{ab} \tilde{S}_i^b, \tag{12}$$

where $\mathbf{R}_i$ and R_i^{ab} are the rotation operator and its matrix representation that takes the direction of magnetic order at site i and rotates it to the z axis of the global coordinate system. With these rotated operators, we can rewrite Eq. (10):

$$H_{\text{spin}} = \sum_{ij} \left[R_i^{\mathrm{T}} \Lambda_{ij} R_j \right]^{ab} \tilde{S}_i^a \tilde{S}_j^b, \tag{13}$$

where R^{T} indicates matrix transposition.

After recasting our spin operators in the rotated coordinate system, we are in the position to analyze the spin waves about the AIAO state by applying linear spin-wave theory. First, we rewrite our spin operators in the Holstein-Primakoff bosonic representation:

$$\begin{aligned} &\tilde{S}_i^+ = \sqrt{2s - a_i^\dagger a_i}\, a_i, \quad \tilde{S}_i^- = a_i^\dagger \sqrt{2s - a_i^\dagger a_i}, \\ &\tilde{S}_i^z = s - a_i^\dagger a_i, \end{aligned} \tag{14}$$

where s is the total spin angular momentum and we have introduced four flavors of bosons, one for each sublattice of the pyrochlore unit cell. Next, we expand and truncate the spin Hamiltonian to quadratic order, Fourier transform the bosonic operators, and solve for the resulting excitation spectrum via a Bogoliubov transformation.

Results. We consider the spin-wave spectra obtained from the effective spin Hamiltonian generated by only NN-hopping amplitudes. Adding up to $t' = 0.1t$ NNN-hopping amplitudes (not shown) only leads to small changes (see below). In Fig. 4, we depict the evolution of the spin-wave spectrum as the NN-hopping parameter θ is varied. In the absence of NNN-hopping amplitudes, θ and $\pi - \theta$ yield identical spin-wave spectra. This structure is again related to our choice of angular parametrization: θ and $-\theta$ are related by a basis transformation and should therefore have the same spin-wave spectrum. Moreover, $-\theta \to -\theta + \pi$ is equivalent to $t \to -t$ and $\mathbf{v} \to -\mathbf{v}$, which leaves J, $\mathbf{D}_{ij}$, and Γ_{ij} invariant. Hence, θ and $\pi - \theta$ yield the same spin-wave spectrum, and this fact is noted by assigning each of the plots in Fig. 4 two θ values.

For $\theta_t/2 < \theta < \pi - \theta_t/2$, the spin-wave spectrum is gapped, and the gap decreases as we approach either end point of the interval. At the end points, two of the four bands of the spectrum become both gapless and dispersionless, while outside the end points, the lowest bands become negative in energy, signaling an instability of the AIAO state. The onset of these instabilities is consistent with NN mean-field theory results, which predicts first-order transitions (between the AIAO and the AIAO$'$ phases) at $\theta = \theta_t/2$ and $\theta = \pi - \theta_t/2$.

We note that the degeneracies at the high-symmetry points Γ, X, and W are consistent with the RPA results as they are protected by symmetry. Also, the flat dispersions at the zone boundary (X-W) are also encountered in the present spin-wave calculation. On the other hand, the lowest-energy dispersion along the L-Γ line is absolutely flat in this NN model. However,

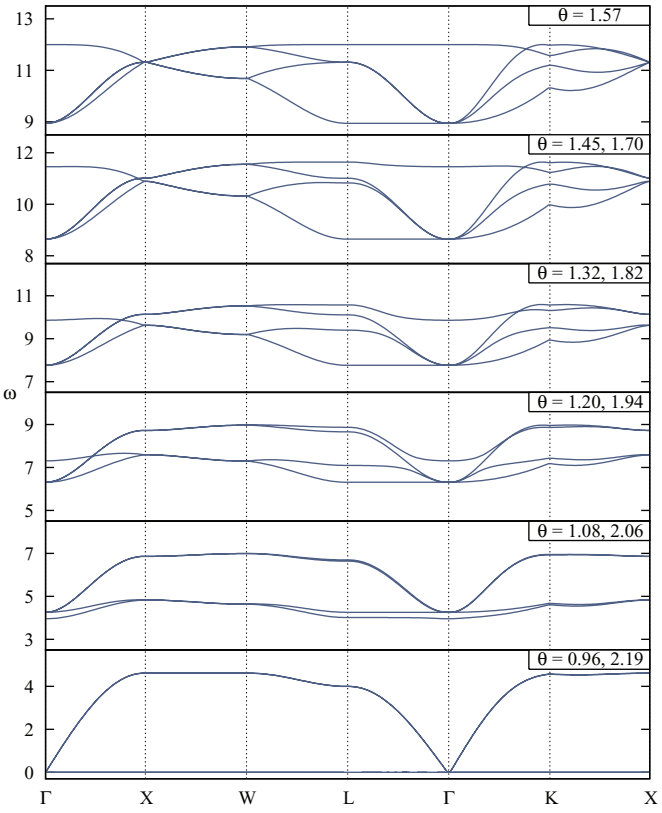

FIG. 4. (Color online) Evolution of the Holstein-Primakoff spin-wave spectra as angle θ is varied between $(\theta_t/2 \approx 0.96) < \theta$ and $\theta < (\pi - \theta_t/2 \approx 2.19)$; ω is in units of t^2/U. θ and $\pi - \theta$ yield identical spin-wave spectra, and this redundancy is reflected by each plot having two θ values. Like the RPA results in Fig. 3, degeneracies at Γ, X, and W are symmetry protected.

on adding small NNN hopping (up to $t' = 0.1t$), it acquires a small dispersion. This should be contrasted with the RPA results in Fig. 3, where modes along the L-Γ line are more strongly dispersive.

C. Comparison of RPA and strong-coupling results

As the ratio of the typical hopping scale to the Hubbard repulsion scale (t/U) increases, the higher-order contributions to the strong-coupling perturbative expansion (in t/U) become increasingly important, and the strictly NN model we employed in Sec. IV B becomes inadequate to describe the magnetic excitations of the AIAO state. Not only do higher-order contributions generate farther-neighbor Heisenberg exchanges, ring-exchange-type terms arise and lead to renormalization of NN quadratic terms at the linear spin-wave level.[39,40] Therefore, we should not expect a perfect agreement between the RPA and strong-coupling results.

Nevertheless, we attempt to fit (by eye estimation) the RPA results for large U (e.g., $U = 6.0$ in cut B) with a linear spin-wave (LSW) spectrum (see Fig. 5). First, we fit the RPA dispersion features and overall bandwidth, resulting in $J = 0.13$, $|\mathbf{D}| = 0.13$, $|\Gamma| = 0.07$ [see Eq. (11) for definitions]. These parameter values are different from those obtained from Eq. (11), which is based strictly on the leading-order

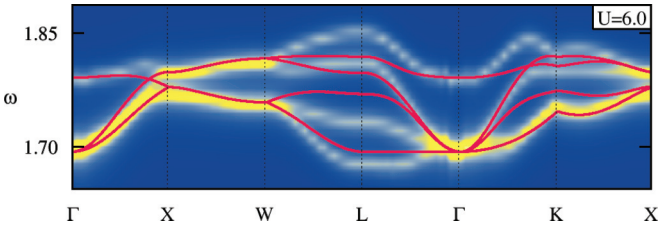

FIG. 5. (Color online) RPA results at $U = 6.0$ for cut B (blue and yellow color map) overlaid with a fit with the NN linear spin-wave spectrum (red); ω is in units of $t = 1$. Although some features along the Γ-X-W line can be fitted, other high-symmetry lines show a larger discrepancy.

strong-coupling expansion for the NNs. The gap obtained from the RPA calculation is $\Delta_{\mathrm{RPA}} \approx 1.70$.

The resulting LSW fit captures the dispersion along Γ-X-W quite well but fails to capture the low-lying modes along the L-Γ line and, in general, the higher-energy modes where the fit, at best, is qualitative. We would also like to point out that fits at lower U and along cut A have been attempted, but large discrepancies in both the features of the spectrum and the spin-wave gap have been found.

The above fitting results point out that the NN spin model (and also the NNN spin model with up to 10% NNN hopping amplitude) is grossly inadequate to fit the RPA magnetic excitation spectrum quantitatively for parameter values that encompass the regime appropriate for the pyrochlore iridates. In this context we would like to point out that recent estimates of a small charge gap (∼10 meV) from the resistivity measurements in $Eu_2Ir_2O_7$[11,25] seem to suggest that the intermediate-coupling calculations may be better suited to describe this compound.

V. SUMMARY

To summarize, we have calculated the structure of the magnetic excitation spectrum for the AIAO state that has been proposed for the pyrochlore iridates such as $Eu_2Ir_2O_7$ and $Y_2Ir_2O_7$. For intermediate correlations, we have calculated the transverse spin-spin dynamical structure factor within the RPA approximation. Features particular to the AIAO configuration that can lead to conclusive identification of the magnetic order in $Eu_2Ir_2O_7$ and $Y_2Ir_2O_7$ were discussed. For the large-U limit, we used a strong-coupling expansion to derive a spin model and calculated the linear spin-wave spectrum using the Holstein-Primakoff approximation. By fitting the RPA results with the linear spin-wave spectrum, we showed that results in the intermediate-correlation regime are substantially different from those obtained from the strong-coupling theory.

Finally, from our calculations, we can make rough estimates of the experimental energy scales for the excitation gap and dispersion bandwidth by using Slater-Koster parametrization of orbital overlaps [the relation connecting the symmetry-allowed parameters in Eq. (6) to Slater-Koster parameters are detailed in Appendix A]. Similar to Refs. 3 and 34, we have used $t_\pi = -2t_\sigma/3$, $t_\delta = 0$, while $t_\sigma = -1.16t_o$ $(-1.37t_o)$ for cut A (B) (the different orbital overlaps were introduced towards the end of Sec. II and are also used in Appendix A). Typically, the value of t_o, the Ir-O-Ir hopping, is about 200–350 meV

in iridates with octahedral oxygen environments.[41,42] Here we choose a representative value of $t_o \approx 300$ meV. The NNN orbital overlaps are more difficult to estimate. However, they are generally much smaller due to the increased interatomic distances and should therefore be consistent with our choice of $t'/t = 0.1$. With these values, in Fig. 3, the spin gap found from our RPA calculation is on the order of 100 meV, and the dispersion width is on the order of ∼15 meV. This value of spin gap is found to be very sensitive to the value of U, while the bandwidth always remains in the same regime. While a 100-meV gap can be resolved within current RIXS resolution, the dispersion width may be presently on the borderline of resolvability.

In other iridium compounds, recent progress has been made in RIXS,[30,31,43] neutron-scattering,[32,44] resonant magnetic x-ray scattering (RMXS),[45,46] and x-ray absorption spectroscopy (XAS)[47] experiments. In particular, RIXS and inelastic neutron-scattering experiments have recently revealed the magnetic excitation spectra of Sr_2IrO_4,[30] $Sr_3Ir_2O_7$,[31] and Na_2IrO_3.[32] Future applications of these techniques and improvements in experimental resolution may help reveal the magnetic behavior and, in particular, the magnetic excitation spectra of pyrochlore iridates, thereby conclusively determining the nature of their magnetic order.

ACKNOWLEDGMENTS

We thank W. Witczak-Krempa, A. Go, Y.-J. Kim, P. Clancy, and B. J. Kim for useful discussion. This research was supported by NSERC, CIFAR, and the Centre for Quantum Materials at the University of Toronto. Computations were performed on the gpc supercomputer at the SciNet HPC Consortium.[48] SciNet is funded by the Canada Foundation for Innovation under the auspices of Compute Canada, the Government of Ontario, Ontario Research Fund–Research Excellence, and the University of Toronto.

APPENDIX A: MICROSCOPIC ORIGINS OF HOPPING PARAMETERS

In order to estimate the values of the hopping parameters, we turn to a microscopic analysis of hopping paths. We briefly discuss the results of such an analysis and refer to Refs. 5,6 and 34 for more details.

We consider two types of hopping: Ir-Ir hopping via overlap of d orbitals and O-Ir hopping between p orbitals of O and d orbitals of Ir. We parametrize d-d overlaps with Slater-Koster amplitudes t_σ, t_π, and t_δ (and primed ones for NNN), while for p-d overlaps, we parametrize them with amplitudes $t_{pd\sigma}$, $t_{pd\pi}$, and O-Ir occupation energy difference ϵ. Here the subscripts σ,π, and δ denote the type of overlap of the orbitals. Also, in this microscopic picture, we always work in the local axes defined by the oxygen octahedra surrounding each Ir.

To arrive at a $J_{\rm eff} = 1/2$ model, we first employ second-order perturbation on the O-Ir hopping to generate an effective NN Ir-Ir hopping between d orbitals. This *indirect* hopping is given by

$$t_{\rm o} = t_{pd\pi}^2/|\epsilon|, \tag{A1}$$

where ϵ is the difference of the on-site charging energies between the oxygen $2p$ orbitals and Ir $5d$ orbitals. (This indirect hopping receives a contribution from the $t_{pd\sigma}$ overlap in the presence of distortion in the oxygen octahedra). We now project the d orbitals into the local t_{2g} and, finally, into the local $J_{\rm eff} = 1/2$ basis to find the hopping matrix which has the form given by Eq. (6), where the relation with the effective hopping parameters and more microscopic Slater-Koster parameters is given by the following relations:

$$\begin{aligned}
t_1 &= \frac{1}{972}(51t_\sigma - 316t_\pi - 43t_\delta + 520t_{\rm o}),\\
t_2 &= \frac{\sqrt{2}}{972}(60t_\sigma - 160t_\pi - 220t_\delta + 112t_{\rm o}),\\
t_1' &= \frac{1}{8748}(699t_\sigma' - 1628t_\pi' - 1843t_\delta'),\\
t_2' &= \frac{\sqrt{2}}{8748}(-156t_\sigma' - 2720t_\pi' - 4t_\delta'),\\
t_3' &= \frac{1}{8748}(-144t_\sigma' - 960t_\pi' + 1104t_\delta').
\end{aligned} \tag{A2}$$

From these relations, it is straightforward to use Eqs. (7) and (8) to relate the angular parameters to the above Slater-Koster parameters.

The range of physical NN hopping parameters explored in Ref. 34 ($-1.2 \lesssim t_\sigma \lesssim -0.5$, $t_\pi = -2t_\sigma/3$, $t_\delta = 0$, and $t_o = 1$) corresponds to $0.85 \lesssim \theta \lesssim 1.51$ with the appropriate energy scaling of t.

APPENDIX B: TRANSVERSE SPIN-SPIN SUSCEPTIBILITY

As Eq. (9) indicates, we need to compute the mean-field transverse spin-spin susceptibility in order to obtain the RPA susceptibility. Here we provide details of such a calculation for noncollinear magnetic order like the AIAO state.

The mean-field susceptibility matrix is given by

$$\chi^{ab}_{{\rm MF}\perp}(\mathbf{q},t) = -i\Theta(t)\langle[(\mathbf{S}^a_\perp(\mathbf{q},t))_i,(\mathbf{S}^b_\perp(-\mathbf{q},0))_i]\rangle, \tag{B1}$$

where $\mathbf{S}^a_\perp(\mathbf{q},t)$ denotes the Fourier transform of the component of the spin operator that is perpendicular to the magnetic ordering direction for sublattice a (see Fig. 1 for sublattice convention) and i indexes the components of $\mathbf{S}^a_\perp(\mathbf{q},t)$, which are to be summed over. If the direction of magnetic moment on sublattice is given by the unit vector $\hat{n}^a$, then the transverse spin operator for that sublattice is given by

$$\mathbf{S}^a_\perp(\mathbf{q}) = -\hat{n}^a \times [\hat{n}^a \times \mathbf{S}^a(\mathbf{q})], \tag{B2}$$

where $\mathbf{S}^a(\mathbf{q})$ is the Fourier transform of the spin operator. For the AIAO state, $\hat{n}^a$ points along the local [111] direction of the lattice.

We write the spin operator with electron operators as

$$\mathbf{S}^a(\mathbf{q}) = \frac{1}{2}\sum_{\mathbf{k}} c^\dagger_{\mathbf{k}+\mathbf{q},\alpha}\boldsymbol{\sigma}_{\alpha\beta}c_{\mathbf{k},\beta}, \tag{B3}$$

where $\alpha,\beta = \uparrow, \downarrow$. Using this, we get

$$\begin{aligned}
\chi^{ab}_{{\rm MF}\perp}(\mathbf{q},t) = -i\,M^{ab}_{\alpha\beta\gamma\delta}\Theta(t)\sum_{\mathbf{k}_1\mathbf{k}_2}\langle[c^\dagger_{a\alpha}(\mathbf{q}+\mathbf{k}_1,t)c_{a\beta}(q_1,t),\\
\times c^\dagger_{b\gamma}(-\mathbf{q}+\mathbf{k}_2,0)c_{b\delta}(\mathbf{k}_2,0)]\rangle,
\end{aligned} \tag{B4}$$

with

$$M^{ab}_{\alpha\beta\gamma\delta} = \tfrac{1}{2}[\hat{n}^a \times (\hat{n}^a \times \sigma_{\alpha\beta})] \cdot \tfrac{1}{2}[\hat{n}^b \times (\hat{n}^b \times \sigma_{\gamma\delta})]. \quad \text{(B5)}$$

Last, we transform our basis to the band basis using the results from our Hartree-Fock mean-field calculation, evaluate the two-body expectation value via Wick's theorem, and Fourier transform to frequency space to obtain $\chi^{ab}_{\mathrm{MF}\perp}(\mathbf{q},\omega)$.

We next compute the trace of the imaginary part of the RPA dynamical structure factor. This trace is a sum of intensities contributed by all four individual magnetic excitation bands and is the quantity most relevant to scattering experiments. From Eq. (9), we notice that $\chi^{ab}_{\mathrm{RPA}\perp}$ has the same eigenbasis as $\chi^{ab}_{\mathrm{MF}\perp}$ since U is diagonal in the sublattice indices. Hence, Eq. (9) can also be regarded as a relation between the eigenvalues of $\chi^{ab}_{\mathrm{RPA}\perp}$ and $\chi^{ab}_{\mathrm{MF}\perp}$. To compute the trace of $\chi^{ab}_{\mathrm{RPA}\perp}$, we therefore diagonalize $\chi^{ab}_{\mathrm{MF}\perp}$ at every $\mathbf{q}$ and ω and use Eq. (9) to compute the eigenvalues of $\chi^{ab}_{\mathrm{RPA}\perp}$.

[1] Y. Machida, S. Nakatsuji, S. Onoda, T. Tayama, and T. Sakakibara, Nature (London) **463**, 210 (2010).
[2] Y. Machida, S. Nakatsuji, Y. Maeno, T. Tayama, T. Sakakibara, and S. Onoda, Phys. Rev. Lett. **98**, 057203 (2007).
[3] W. Witczak-Krempa and Y. B. Kim, Phys. Rev. B **85**, 045124 (2012).
[4] A. Go, W. Witczak-Krempa, G. S. Jeon, K. Park, and Y. B. Kim, Phys. Rev. Lett. **109**, 066401 (2012).
[5] B.-J. Yang and Y. B. Kim, Phys. Rev. B **82**, 085111 (2010).
[6] D. Pesin and L. Balents, Nat. Phys. **6**, 376 (2010).
[7] X. Wan, A. M. Turner, A. Vishwanath, and S. Y. Savrasov, Phys. Rev. B **83**, 205101 (2011).
[8] B. J. Kim, H. Jin, S. J. Moon, J.-Y. Kim, B.-G. Park, C. S. Leem, J. Yu, T. W. Noh, C. Kim, S.-J. Oh, J.-H. Park, V. Durairaj, G. Cao, and E. Rotenberg, Phys. Rev. Lett. **101**, 076402 (2008).
[9] B. J. Kim, H. Ohsumi, T. Komesu, S. Sakai, T. Morita, H. Takagi, and T. Arima, Science **323**, 1329 (2009).
[10] K. Matsuhira, M. Wakeshima, Y. Hinatsu, and S. Takagi, J. Phys. Soc. Jpn. **80**, 094701 (2011).
[11] S. Zhao, J. M. Mackie, D. E. MacLaughlin, O. O. Bernal, J. J. Ishikawa, Y. Ohta, and S. Nakatsuji, Phys. Rev. B **83**, 180402 (2011).
[12] H. Fukazawa and Y. Maeno, J. Phys. Soc. Jpn. **71**, 2578 (2002).
[13] N. Aito, M. Soda, Y. Kobayashi, and M. Sato, J. Phys. Soc. Jpn. **72**, 1226 (2003).
[14] S. Nakatsuji, Y. Machida, Y. Maeno, T. Tayama, T. Sakakibara, J. van Duijn, L. Balicas, J. N. Millican, R. T. Macaluso, and J. Y. Chan, Phys. Rev. Lett. **96**, 087204 (2006).
[15] M. Kargarian, J. Wen, and G. A. Fiete, Phys. Rev. B **83**, 165112 (2011).
[16] R. S. Singh, V. R. R. Medicherla, K. Maiti, and E. V. Sampathkumaran, Phys. Rev. B **77**, 201102 (2008).
[17] M. Kurita, Y. Yamaji, and M. Imada, J. Phys. Soc. Jpn. **80**, 044708 (2011).
[18] S. M. Disseler, C. Dhital, T. C. Hogan, A. Amato, S. R. Giblin, C. de la Cruz, A. Daoud-Aladine, S. D. Wilson, and M. J. Graf, Phys. Rev. B **85**, 174441 (2012).
[19] S. M. Disseler, C. Dhital, A. Amato, S. R. Giblin, C. de la Cruz, S. D. Wilson, and M. J. Graf, Phys. Rev. B **86**, 014428 (2012).
[20] F. F. Tafti, J. J. Ishikawa, A. McCollam, S. Nakatsuji, and S. R. Julian, Phys. Rev. B **85**, 205104 (2012).
[21] G. Chen and M. Hermele, Phys. Rev. B **86**, 235129 (2012).
[22] D. Yanagishima and Y. Maeno, J. Phys. Soc. Jpn. **70**, 2880 (2001).
[23] N. Taira, M. Wakeshima, and Y. Hinatsu, J. Phys. Condens. Matter **13**, 5527 (2001).
[24] K. Matsuhira, M. Wakeshima, R. Nakanishi, T. Yamada, A. Nakamura, W. Kawano, S. Takagi, and Y. Hinatsu, J. Phys. Soc. Jpn. **76**, 043706 (2007).
[25] J. J. Ishikawa, E. C. T. O'Farrell, and S. Nakatsuji, Phys. Rev. B **85**, 245109 (2012).
[26] K. Tomiyasu, K. Matsuhira, K. Iwasa, M. Watahiki, S. Takagi, M. Wakeshima, Y. Hinatsu, M. Yokoyama, K. Ohoyama, and K. Yamada, J. Phys. Soc. Jpn. **81**, 034709 (2012).
[27] M. Sakata, T. Kagayama, K. Shimizu, K. Matsuhira, S. Takagi, M. Wakeshima, and Y. Hinatsu, Phys. Rev. B **83**, 041102 (2011).
[28] M. C. Shapiro, S. C. Riggs, M. B. Stone, C. R. de la Cruz, S. Chi, A. A. Podlesnyak, and I. R. Fisher, Phys. Rev. B **85**, 214434 (2012).
[29] M. Elhajal, B. Canals, R. Sunyer, and C. Lacroix, Phys. Rev. B **71**, 094420 (2005).
[30] J. Kim, D. Casa, M. H. Upton, T. Gog, Y.-J. Kim, J. F. Mitchell, M. van Veenendaal, M. Daghofer, J. van den Brink, G. Khaliullin, and B. J. Kim, Phys. Rev. Lett. **108**, 177003 (2012).
[31] J. Kim, A. H. Said, D. Casa, M. H. Upton, T. Gog, M. Daghofer, G. Jackeli, J. van den Brink, G. Khaliullin, and B. J. Kim, Phys. Rev. Lett. **109**, 157402 (2012).
[32] S. K. Choi, R. Coldea, A. N. Kolmogorov, T. Lancaster, I. I. Mazin, S. J. Blundell, P. G. Radaelli, Y. Singh, P. Gegenwart, K. R. Choi, S.-W. Cheong, P. J. Baker, C. Stock, and J. Taylor, Phys. Rev. Lett. **108**, 127204 (2012).
[33] T. Moriya, Phys. Rev. **120**, 91 (1960).
[34] W. Witczak-Krempa, A. Go, and Y. B. Kim, Phys. Rev. B **87**, 155101 (2013).
[35] S. Bhattacharjee, S.-S. Lee, and Y. B. Kim, New J. Phys. **14**, 073015 (2012).
[36] P. Buczek, A. Ernst, and L. M. Sandratskii, Phys. Rev. B **84**, 174418 (2011).
[37] P. Mohn, *Magnetism in the Solid State: An Introduction* (Springer, New York, 2003).
[38] K. A. Ross, L. Savary, B. D. Gaulin, and L. Balents, Phys. Rev. X **1**, 021002 (2011).
[39] A. L. Chernyshev, D. Galanakis, P. Phillips, A. V. Rozhkov, and A.-M. S. Tremblay, Phys. Rev. B **70**, 235111 (2004).
[40] J.-Y. P. Delannoy, M. J. P. Gingras, P. C. W. Holdsworth, and A.-M. S. Tremblay, Phys. Rev. B **72**, 115114 (2005).
[41] M. R. Norman and T. Micklitz, Phys. Rev. B **81**, 024428 (2010).
[42] C. H. Kim, H. S. Kim, H. Jeong, H. Jin, and J. Yu, Phys. Rev. Lett. **108**, 106401 (2012).
[43] H. Gretarsson, J. P. Clancy, X. Liu, J. P. Hill, E. Bozin, Y. Singh, S. Manni, P. Gegenwart, J. Kim, A. H. Said, D. Casa, T. Gog, M. H. Upton, H.-S. Kim, J. Yu, V. M. Katukuri, L. Hozoi, J. van den Brink, and Y.-J. Kim, Phys. Rev. Lett. **110**, 076402 (2013).

[44]F. Ye, S. Chi, H. Cao, B. C. Chakoumakos, J. A. Fernandez-Baca, R. Custelcean, T. F. Qi, O. B. Korneta, and G. Cao, Phys. Rev. B **85**, 180403 (2012).

[45]X. Liu, T. Berlijn, W.-G. Yin, W. Ku, A. Tsvelik, Y.-J. Kim, H. Gretarsson, Y. Singh, P. Gegenwart, and J. P. Hill, Phys. Rev. B **83**, 220403 (2011).

[46]J. P. Clancy, K. W. Plumb, C. S. Nelson, Z. Islam, G. Cao, T. Qi, and Y.-J. Kim (2012), arXiv:1207.0960.

[47]J. P. Clancy, N. Chen, C. Y. Kim, W. F. Chen, K. W. Plumb, B. C. Jeon, T. W. Noh, and Y.-J. Kim, Phys. Rev. B **86**, 195131 (2012).

[48]C. Loken, D. Gruner, L. Groer, R. Peltier, N. Bunn, M. Craig, T. Henriques, J. Dempsey, C.-H. Yu, J. Chen, L. J. Dursi, J. Chong, S. Northrup, J. Pinto, N. Knecht, and R. V. Zon, J. Phys. Conf. Ser. **256**, 012026 (2010).